



# Robust Fe-N<sub>4</sub> center with optimized metal-support interaction for efficient pollutant degradation by Fenton-like reaction

Jiahao Cui<sup>a</sup>, Lina Li<sup>a</sup>, Yucheng Wu<sup>b</sup>, Jingyu Gao<sup>a</sup>, Kun Wang<sup>a</sup>, Caozheng Diao<sup>c</sup>, Chun Hu<sup>a</sup>, Yubao Zhao<sup>a,\*</sup>

<sup>a</sup> Key Laboratory for Water Quality and Conservation of the Pearl River Delta, Ministry of Education & Institute of Environmental Research at Greater Bay, Guangzhou University, 510006 Guangzhou, PR China

<sup>b</sup> College of Civil Engineering, Guangzhou University, 510006 Guangzhou, PR China

<sup>c</sup> Singapore Synchrotron Light Source, National University of Singapore, 117603, Singapore

## ARTICLE INFO

### Keywords:

Fenton-like reaction  
High-valent iron-oxo species  
Pollutant degradation  
Single-atom catalysis  
Iron chemistry

## ABSTRACT

Single-atom Fe catalysis has exhibited remarkable potentials in water treatment applications. However, rational design of single-atom Fe catalysts with controlled catalytic performance is still challenging, due to the lack of the fundamental understanding on the correlated factors of structure, property, and catalytic behavior. Herein, PMS activation performance of the single-atom Fe sites is successfully boosted by molecular-engineering on the polymeric carbon nitride (CN) framework. Benzene-1,4-diamine regulates the polymerization process, and rises the ratio of carbon/nitrogen; the valence of the single-atom Fe is thereby positively shifted, leading to favorable thermal dynamics of the high-valent Fe(IV)=O involved oxidation reaction. The carbon-rich CN supported single-atom Fe catalyst thus exhibits remarkable performance in selective degradation of a series of organic pollutants via high-valent Fe(IV)=O oxidation pathway. The findings in this work implicate the significance of electronic properties of the support as one of the essential descriptors for a robust single-atom catalyst for pollutants abatement.

## 1. Introduction

Peroxymonosulfate (PMS)-based advanced oxidation process (AOP) is a promising technology for water treatment [1–6]. Among various reactive species generated in AOP, the high-valent Fe(IV)=O exhibits mild oxidation power, high steady-state concentration ( $> 9.76 \times 10^{-9}$  M), and relatively longer life time ( $\sim 0.1$  s, at pH 3) as compare to the radicals [7,8]. The high-valent Fe(IV)=O species is thus an ideal candidate for the selective degradation of the emerging organic pollutants (EOPs) [9–11], which threaten the human health and the aquatic ecosystem even at ng/L concentration with long term exposure [12–16]. To selectively eliminate the EOPs in the complex water matrix, it is urgent to develop robust and selective catalysts, which could efficiently generate the high-valent Fe(IV)=O species.

In biological metabolism, the heme/non-heme complexed iron in enzymes can produce high-valent Fe(IV)=O, which is the active species for selective oxidative transformations [17,18]. Most importantly, the electronic properties of the ligands have been revealed to directly impact the catalytic activity of the metal center [19,20]. In recent years,

single-atom catalysis (SAC) has been one of the frontiers in heterogeneous catalysis [21–27]; it is promising in both mechanistic understanding on catalysis and practical applications, due to the unique advantages of utmost metal-atoms utilization efficiency and the well-defined structural configurations of the metal sites [28]. The supported single-atom Fe catalysts resemble the structure of the configurations of Fe-N<sub>4</sub> in iron porphyrins and phthalocyanines in bio-catalysis, potentially being able to generate the high-valent iron-oxo species [22, 29]. Accordingly, it is highly expected to finely tune the catalytic activity of the single-atom Fe sites by regulating the molecular structure of the support, i.e., to optimize the catalytic performance of the single-atom Fe center by modulating the metal-support interaction (MSI) [30,31]. Therefore, it is critical to select a suitable support for the single-atom catalyst.

Polymeric carbon nitride (CN) framework, a stable and non-toxic porous material with earth-abundant composition, is an ideal support for anchoring the single-atom metals, due to its unparalleled feature of nitrogen-richness [32,33]. It is especially worth noting that CN has a modular structure, i.e., the architecture of CN could be precisely tuned

\* Corresponding author.

E-mail address: [yubaozhao@gzhu.edu.cn](mailto:yubaozhao@gzhu.edu.cn) (Y. Zhao).

<https://doi.org/10.1016/j.apcatb.2023.122706>

Received 28 December 2022; Received in revised form 10 March 2023; Accepted 28 March 2023

Available online 5 April 2023

0926-3373/© 2023 Elsevier B.V. All rights reserved.

on molecular-level [34–38]. In addition, the metal-support interaction links the single-atom metal sites and the supports; as such, there are rich opportunities for regulating the catalytic activity of the CN supported single-atom Fe sites by structural engineering of the CN framework. Organic amines could regulate the nucleation and crystallization process of zeolite imidazolate frameworks (ZIF) by competing with the bridging ligand [39]. Benzene-1,4-diamine (BDA) with *para*-positioned amino groups, is expected to be a suitable building block for molecular-engineering on the CN support.

Herein, we demonstrate the unique role of BDA in tuning the polymerization process, and creating carbon-rich CN supported single-atom Fe catalyst via a one-step synthesis. The carbon-rich nature of the support lowers the electron density of the single-atom Fe sites, thermodynamically favoring the oxygen-atom transfer from the high-valent Fe(IV)=O to the organic molecule. As a consequence, the carbon-rich CN framework supported single-atom Fe catalyst exhibited superior catalytic performance in catalytic degradation of the EOPs in the presence of PMS via high-valent Fe(IV)=O oxidation pathway.

## 2. Experimental procedures

### 2.1. Synthesis of the single-atom Fe catalysts

The construction of the polymeric carbon nitride framework was based on the reported method of polymerization of the super-molecular assembly of melamine and cyanuric acid [40]. To synthesize the polymeric carbon nitride supported single-atom Fe catalysts, benzene-1,4-diamine (BDA, the amount was denoted by *x*, and *x* = 0, 0.25, 0.5, 0.75 g), FeCl<sub>3</sub>·6 H<sub>2</sub>O (6.0 mmol), chitosan (CS, 0.5 g), cyanuric acid (CA, 5 g), and melamine (MA, 5 g) were dispersed in 200 mL of water, and mixed under magnetic stirring at room temperature overnight. The precursor was dried in an oven at 120 °C; and the thermal polymerization reaction was conducted in a tube furnace with nitrogen flow at 600 °C for 2 h. The as-prepared samples were immersed in 0.5 M H<sub>2</sub>SO<sub>4</sub> solution for 12 h under room temperature, followed by washing with water until the filtrate being neutral in pH. The polymeric carbon nitride supported single-atom Fe catalysts denoted by *Fe<sub>1</sub>-CN* and *Fe<sub>1</sub>-CN-BDA<sub>x</sub>* were then collected and dried in a vacuum oven.

### 2.2. Evaluation of the catalytic performance

In a typical experiment of catalytic PMS activation for the pollutant degradation, 5 mg catalyst was dispersed in 25 mL BPA solution by ultrasonication for 10 min, followed by mixing by magnetic stirrer in dark for 15 min to reach the adsorption-desorption equilibrium. It has been experimentally confirmed that 15 min was more than enough for reaching the equilibrium. The suspension was sampled for initial BPA concentration analysis. The catalytic reaction was initiated by dropping the PMS stock solution (1 M), and the initial PMS concentration was 1 mM, unless otherwise stated. The suspension was sample at specific intervals, the catalyst was removed by syringe filter, and the filtrated was mixed with methanol for pollutants concentration analysis with HPLC. If not specified, the initial pH of the solution was around 6.5. HPLC analysis were performed on Shimadzu SIL-20A HPLC with Shim-pack GIST C18 column (4.6 × 250 mm, 5 μm). Mobile phase and detection wavelength setting for the pollutants: bis phenol A (BPA), methanol/water (70/30) and λ = 225 nm; sulfamethoxazole, methanol/water (55/45) and λ = 266 nm; 4-chloro-phenol, phosphate acid solution (0.08%)/acetonitrile (50/50) and λ = 221 nm; methyl phenyl sulfoxide (MPSO), phosphate acid solution (0.08%)/acetonitrile (70/30) and λ = 215 nm.

## 3. Results and discussion

### 3.1. Evaluation of the performance of the single-atom catalysts

The molecular configuration of the support for the single-atom Fe catalyst was modulated via introducing BDA into the super-molecular assembly of melamine and cyanuric acid. The thermal polymerization reaction converted the super-molecular assembly into polymeric carbon nitride (CN) supported single-atom Fe catalysts. Adjusting the amount of BDA in the super-molecular assembly generated a series of single-atom Fe catalysts, which were denoted by *Fe<sub>1</sub>-CN-BDA<sub>x</sub>* (*x*, the amount of BDA in the precursor). *Fe<sub>1</sub>-CN* was synthesized in the absence of BDA.

The impact of the configurations of the support on the catalytic performance was visualized by applying in the catalytic degradation of bisphenol A (BPA) in the presence of PMS. On *Fe<sub>1</sub>-CN*, 60% of BPA is removed at the reaction time of 180 s. The catalytic performance increases with the amount of BDA in the precursor; and *Fe<sub>1</sub>-CN-BDA0.75* exhibits a remarkable activity, eliminating BPA within 120 s. The pseudo first-order reaction rate constant of the *Fe<sub>1</sub>-CN-BDA0.75* catalyzed reaction reaches a high value of 0.045 s<sup>-1</sup>, which is 5.1 times of that in the *Fe<sub>1</sub>-CN* catalyzed reaction system (Fig. 1a, b). The main intermediates during BPA degradation by *Fe<sub>1</sub>-CN-BDA0.75* are identified with mass spectrometer (Table S1). At the reaction time of 180 s in a batch reaction, the TOC removal reaches a high value of 79.8%, which may result from the combination of mineralization and polymerization of the intermediates [3]. The equal amount of Fe<sup>3+</sup> and Iron phthalocyanine (Fe-PC) were selected as the comparisons performance with *Fe<sub>1</sub>-CN-BDA0.75*, and the results highlight the excellent catalytic performance of *Fe<sub>1</sub>-CN-BDA0.75* in PMS activation (Fig. S1). And The optimum catalyst of *Fe<sub>1</sub>-CN-BDA0.75* was applied in degradation of a couple of selected refractory organic pollutants of concern to the public (Figs. 1c and S2) [41]. Chlorophenol and 2,4-dichlorophenol, two representative organohalide pollutants, are eliminated within a short reaction time of 60 s. Sulfamethoxazole (SMX) and phenol, can be degraded at a reaction rate lower than that of BPA, for instance, 80% SMX removal and 84% phenol removal at the reaction time of 180 s. The terephthalic acid (TPA), with two electron-withdrawing carboxylic group on the benzene ring, is unable to be degraded in this reaction system. Obviously, the single-atom Fe catalyzed PMS activation system here is mild in oxidizing power, and is especially suitable for selective elimination of the organic pollutant with electron-rich moieties. The impact of the mineral ions and humic acid on the BPA degradation in the *Fe<sub>1</sub>-CN-BDA0.75* catalyzed reaction system was thereafter examined. As shown in Fig. 1d, in the presence of a series of typical mineral ions with concentration of 5 mM, BPA could be eliminated efficiently. Additionally, the impact of the natural organic matters (NOMs) on the performance of the catalyst is demonstrated by analyzing the BPA degradation performance in the presence of 5 ppm humic acid, revealing a desired resistance to the interference from humic acid in this reaction system. Obviously, *Fe<sub>1</sub>-CN-BDA0.75* catalyzed reaction system owns well tolerance on the mineral ions and natural organic matters, which is of importance to the selective removal of the EOPs in the real water matrix.

The stability of the catalyst was measured in flow mode in a fixed-bed reactor [42]. With *Fe<sub>1</sub>-CN-BDA0.75* loaded, the column can run stably for 84 h with 100% BPA removal for treating the influent with 0.1 mM of BPA concentration (Fig. 1e), corresponding to a water treatment capacity of 40 L per 1 g of catalyst. The concentration of leached Fe ions in the effluent is below 2 ppm, which is no harm for the aquatic environment.

### 3.2. Structural analysis of the single-atom catalyst

For exploring the rationale behind the boost of the catalytic performance by structural engineering of the support, selected single-atom Fe catalysts were systematically characterized by a series of microscopic and spectroscopic techniques. Scanning electron microscopy (SEM)

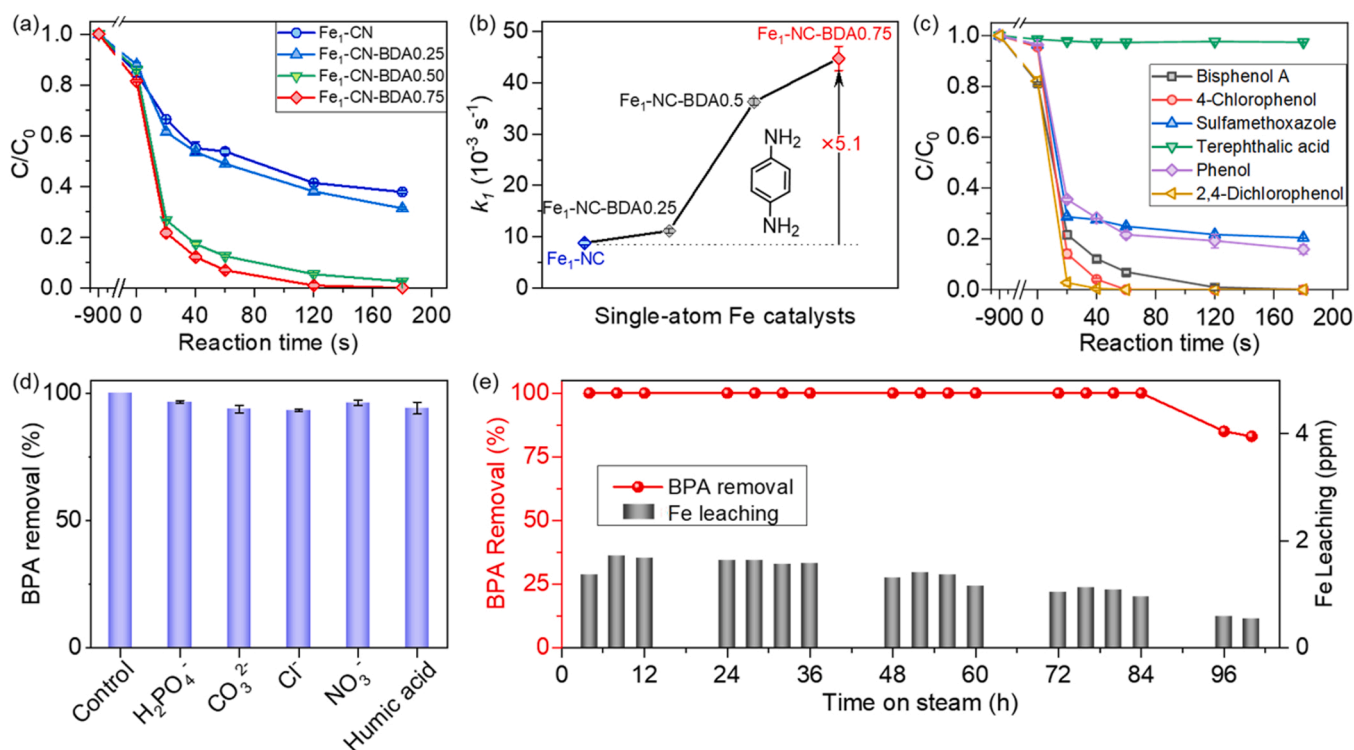


**Fig. 1.** (a) Degradation of BPA by the single-atom Fe catalysts with engineered supports by 1,4-Benzenediamine. (b) The pseudo-first order reaction rate constants of the reaction catalyzed by the single-atom Fe catalysts. (c) The degradation of a series organic pollutants. (d) The impact of the mineral ions and humic acid on the catalytic performance of Fe<sub>1</sub>-CN-BDA0.75 for BPA removal. Reaction time = 180 s (e) Catalytic performance of Fe<sub>1</sub>-CN-BDA0.75 in a fixed-bed flow reactor for BPA removal. Reaction conditions for (a), (c), and (d): [catalyst] = 0.20 g L<sup>-1</sup>, [PMS] = 1.0 mM, initial pH = 6.5, [ions] = 5.0 mM (if any), [humic acid] = 5 mg L<sup>-1</sup> (if any). Flow reaction: catalyst loadings: 50 mg, [BPA] = 0.1 mM, [PMS] = 1.0 mM, flow rate = 24 mL h<sup>-1</sup>.

images reveal that the introduction of BDA in the precursor of the catalyst regulated the nucleation and growth of the CN framework, and thus shaped the nanoarchitecture of the CN support. For instance, Fe<sub>1</sub>-CN-BDA0.75 shows a sheet-like structure much thinner than that of Fe<sub>1</sub>-CN (Fig. 2a). In transmission electron microscopy (TEM) image, Fe<sub>1</sub>-CN-BDA0.75 is in a very thin sheet-like morphology (Fig. 2b), and no metal nano-particles are observed. However, the impact of the slight difference in specific surface area on performance is excluded (Table S2). By energy-dispersive X-ray spectroscopy (EDS) mapping, the elements of N, C, O, and Fe in the catalyst are visualized (Fig. 2b); and all the elements are uniformly dispersed throughout the CN matrix. Surprisingly, although Fe<sub>1</sub>-CN and Fe<sub>1</sub>-CN-BDA0.75 are significantly distinct in the catalytic activity, their Fe loadings are almost the same, 5.7 and 6.1 wt% respectively for the former and the latter, as determined by inductively coupled plasma atomic emission spectroscopy (ICP-OES) (Table S3). This intrigues us to further explore the key factors that are determining the catalytic performance.

Fourier transform infrared (FT-IR) and X-ray diffraction (XRD) spectra reflect the typical structural features of the CN framework. As shown in Fig. S3, the absorption peak at 808 cm<sup>-1</sup> is due to the out-of-plane bending of the tri-s-triazine unit. Strong and broad absorption peaks at 3000 cm<sup>-1</sup> to 3500 cm<sup>-1</sup> are observed and assigned to the N–H/O–H stretching vibration [43]. The asymmetric vibration signal of cyano group appears at 2175 cm<sup>-1</sup>. In Fig. S4, the diffraction peak of Fe<sub>1</sub>-CN at 27.5° is attributed to the layer stackings structure on (001) direction with interlayer spacing of 0.33 nm [40,44,45].

X-ray photoelectron spectroscopy (XPS) was employed for further analyzing the chemical structures of the single-atom Fe catalysts. XPS survey scan reveals the elemental composition of N, C, Fe, and O (Fig. S5). As shown in Fig. 2c, the C 1s signal is deconvoluted into 4 components at 288.6, 287.7, 286.3, and 284.8 eV, which are assigned to C=N/C=O, N–C=N in the heptazine unit, C–C, and carbon-carbon

bond in sp<sup>2</sup> configuration (C=C), respectively [46,47]. The polymerization reaction regulated by BDA inserts more C–C and C=C units in the CN framework; for instance, the carbon element in C=C configuration accounts for 11.7% and 46.7% of the total carbon elements in the framework of Fe<sub>1</sub>-CN and Fe<sub>1</sub>-CN-BDA0.75, respectively (Table S4).

As shown in Fig. 2d, the N 1s signal is deconvoluted into 3 peaks, 401.0 eV (graphitic N), 400.0 eV (amine group), and 398.6 eV (nitrogen functional forms of pyridinic N and cyano group). For Fe<sub>1</sub>-CN, the 15.1% of the N element is in a configuration of graphitic N, and this value increases to 23.6% in Fe<sub>1</sub>-CN-BDA0.75. Meanwhile, the percentages of N in the triazine unit for Fe<sub>1</sub>-CN and Fe<sub>1</sub>-CN-BDA0.75 are 68.1% and 59.3%, respectively (Table S5). As determined by XPS, the ratios of C/N in Fe<sub>1</sub>-CN and Fe<sub>1</sub>-CN-BDA0.75 are 0.82 and 1.44, respectively (Table S6). The increase of the ratio of C/N by BDA regulation is expected to modulate the electronic structure of CN framework [48]. In the Fe 2p XPS spectra, two main peaks at 710.5 eV and 724.1 eV are, respectively, corresponding to Fe<sup>2+</sup> 2p<sub>3/2</sub> and 2p<sub>1/2</sub> (Fig. S6) [49,50].

Further understanding on the microstructure was strengthened by synchrotron radiation X-ray absorption spectroscopy. Nitrogen K-edge X-ray absorption near-edge structure (XANES) spectra of Fe<sub>1</sub>-CN and Fe<sub>1</sub>-CN-BDA0.75 show multiple  $\pi^*$  resonance peaks in the energy range from 397 to 405 eV (Fig. 2e). The  $\pi^*$  resonances peaks at 401.9 and 403.1 eV result from the amino/amine N, and graphitic N in CN framework, respectively [51,52]. It is worth mentioning that the peaks ascribed to pyridinic N in Fe<sub>1</sub>-CN and Fe<sub>1</sub>-CN-BDA0.75 reveal key structural features [53]. Particularly, the spectrum of Fe<sub>1</sub>-CN has a  $\pi^*$  resonances peak at 400.0 eV, indicating the pyridinic N in the heptazine unit; while in the case of Fe<sub>1</sub>-CN-BDA0.75, there is an additional shoulder peak at 398.8 eV, which results from the pyridinic N in the graphene-like carbon plane [52,54]. All the spectroscopy investigations consistently reveal that the BDA regulation constructs carbon-rich segments in the CN framework.



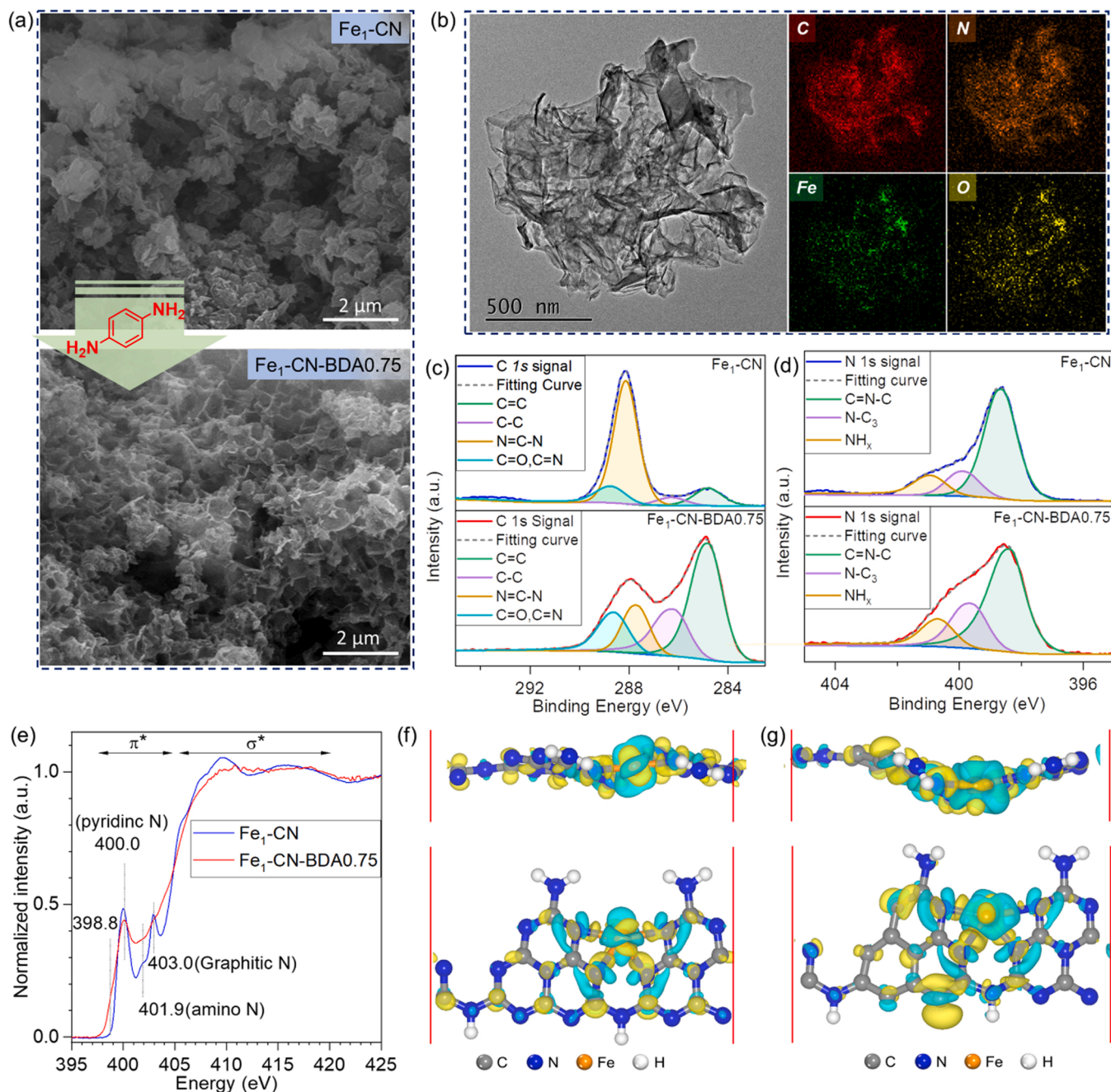


**Fig. 2.** (a) Scanning electron microscopy (SEM) image of Fe<sub>1</sub>-CN and Fe<sub>1</sub>-CN-BDA0.75. (b) Transmission electron microscopy (TEM) images and energy-dispersive X-ray spectroscopy (EDX) mapping of the elements in Fe<sub>1</sub>-CN-BDA0.75. (c, d) X-ray photoelectron spectroscopy (XPS) profiles of C 1s (c) and N 1s (d) signals. (e) N K-edge X-ray adsorption spectra of Fe<sub>1</sub>-CN and Fe<sub>1</sub>-CN-BDA0.75. (f, g) Side and top-view of differential charge density of the elements in Fe<sub>1</sub>-CN (f) and Fe<sub>1</sub>-CN-BDA0.75 (g), wherein the cyan and yellow isosurfaces denote electron accumulation and depletion, respectively.

Based on the structural analysis, a theoretical model of Fe<sub>1</sub>-CN was constructed based on the linear melon structure with repeating heptazine units; and the carbon-rich nature of the BDA regulated catalyst was translated into partial replacing of the N atoms by C atoms in the linear melon configuration (Fig. S7). In the optimized configuration, Fe atoms are coordinating with four pyridinic N atoms, wherein the Fe-N bond is proposed to be the bridge for MIS. Therefore, differential charge density by DFT calculation was conducted to visualize the MSI. Fig. 2f and g demonstrate discrete charges distribution in the single-atom Fe catalyst. Specifically, the charge transfer between the Fe center and surrounding nitrogen atoms is much stronger in Fe<sub>1</sub>-CN-BDA than that in Fe<sub>1</sub>-CN. The regulation of the electronic structure of the Fe center by the carbon-rich support via MSI was thereafter analyzed by Fe K-edge X-ray absorption

spectroscopy (XAS).

We then attempt to explore the configurations of the Fe center in the catalyst with atomic-resolution transmission electron microscope and synchrotron radiation facility. Aberration-corrected high-angle annular dark-field scanning transmission electron microscopy (AC-HAADF-STEM) was employed for visualizing the atomically dispersed Fe in Fe<sub>1</sub>-CN-BDA0.75. The bright spots in Fig. 3a and b demonstrate that Fe atoms present in form of isolated single atoms, and no metal clusters or crystals are detected. Fig. 3c presents the Fe K-edge extended X-ray absorption fine structure (EXAFS) data of Fe<sub>1</sub>-CN, Fe<sub>1</sub>-CN-BDA0.75, and reference samples of Fe<sub>2</sub>O<sub>3</sub>, FeO, and Fe foil. The absorption edges demonstrate the valence of Fe in the samples; and the valence of Fe in Fe<sub>1</sub>-CN, Fe<sub>1</sub>-CN-BDA0.75 is determined to be +2.05 and +2.21,

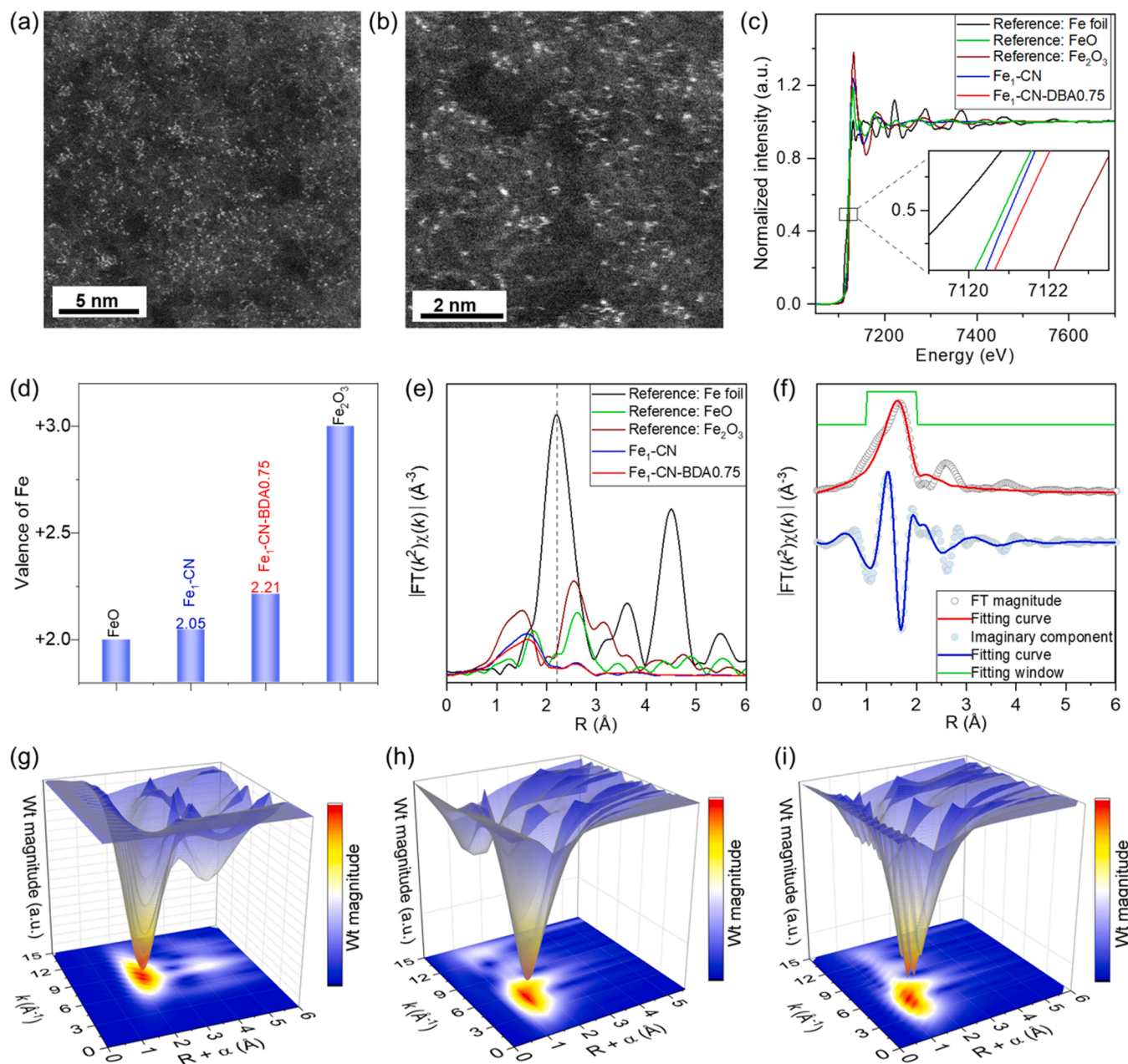


**Fig. 3.** (a, b) Aberration-corrected high-angle annular dark-field scanning transmission electron microscopy (AC-HAADF-STEM) image of  $\text{Fe}_1\text{-CN-BDA0.75}$ . (c) Fe K-edge EXAFS spectra of  $\text{Fe}_1\text{-CN}$  and  $\text{Fe}_1\text{-CN-BDA0.75}$  with reference samples of Fe foil, FeO, and  $\text{Fe}_2\text{O}_3$ . (d) Valence of Fe element in  $\text{Fe}_1\text{-CN}$  and  $\text{Fe}_1\text{-CN-BDA0.75}$  determined by comparing the first-derivative of adsorption profiles of the catalyst with the reference samples. (e) The  $k^2$ -weighted EXAFS spectra in  $R$  space of the single-atom Fe catalysts and the reference samples;  $R$  is the interatomic distance, indicating the radial distance without phase correction.  $\chi(R)$  is the Fourier transform in the  $R$  space. (f) Fe K-edge Fourier transform EXAFS spectrum of  $\text{Fe}_1\text{-CN-BDA0.75}$  and the fitting curves. (g-i) Wavelet transforms of the  $k^2$ -weighted EXAFS of the references of Fe Foil (g),  $\text{Fe}_1\text{-CN}$  (h),  $\text{Fe}_1\text{-CN-BDA0.75}$  (i).

respectively, referring to the valence of Fe in FeO (+2.00) and  $\text{Fe}_2\text{O}_3$  (+3.00) (Fig. 3d). Alteration on the valence of the single-atom Fe site can lead to significant modulation on its catalytic activity [49,55,56].

In the  $k^2$ -weighted Fourier transforms of the EXAFS spectra in the  $R$  space, for both  $\text{Fe}_1\text{-CN}$  and  $\text{Fe}_1\text{-CN-BDA0.75}$ , there is one predominant peak at 1.57 Å, which is assigned to the signal of Fe–N path in the first shell (Fig. 3e) [57–59]. While for the reference of Fe foil, the first-shell Fe–Fe scattering path is at 2.22 Å, and the Fe–Fe path is not exist in the spectra of  $\text{Fe}_1\text{-CN}$  and  $\text{Fe}_1\text{-CN-BDA0.75}$ , confirming the absence of Fe clusters. The peak corresponding to the first-shell scattering path of Fe–O at around 1.5 Å is shown in the curves of  $\text{Fe}_2\text{O}_3$  and FeO [60]. The EXAFS spectrum was further fitted for analyzing the coordination number and the bond length of the central Fe atoms with respect to the

neighbouring atoms. Fitting on Fe–N scattering path in the first shell for  $\text{Fe}_1\text{-CN-BDA0.75}$  states the coordination number of  $\sim 4$  and bond distance of 2.09 Å (Fig. 3f, Table S7).  $\text{Fe}_1\text{-CN}$  has a similar configuration of Fe–N<sub>4</sub> structure to that of  $\text{Fe}_1\text{-CN-BDA0.75}$  (Figs. S8, Table S8).

Wavelet transformation (WT) EXAFS analysis provides not only the radial distance resolution, but also resolves in  $k$  space; it therefore facilitates the discrimination of the atoms by their elemental nature [61, 62]. Fig. 3g shows the WT contour maps for the reference sample of Fe foil, and the intensity maximum is at the  $k$  value of  $8.9 \text{ Å}^{-1}$ . While for the samples of  $\text{Fe}_1\text{-CN}$  and  $\text{Fe}_1\text{-CN-BDA0.75}$ , the contour intensity maxima are, respectively, at the  $k$  value of 5.3 and  $5.2 \text{ Å}^{-1}$  in the WT contour map (Fig. 3h, i). The WT EXAFS analysis repeatedly states that the Fe atoms present as mononuclear centres without involving in a metal



cluster or crystals.

The structural analysis via both microscopic/spectroscopic analysis and theoretical simulation investigations reveals that the BDA regulates the nucleation and polymerization process, introduces carbon-rich moieties in the CN framework in form of graphene-like units; the reduction of the conjugated electron density of the framework positively shift the valence state of Fe center via the bridge of Fe–N bond between the single-atom Fe and CN support. For a further understanding on the structural stability of the catalyst in the reaction, the used Fe<sub>1</sub>-CN-BDA0.75 was analyzed by a series of techniques. The XRD and XPS spectra reveals that there are no obvious changes on the composition and crystal structure of the carbon nitride framework after a reaction (Figs. S9a–S9e). The AC-HAADF-STEM image of the used catalyst indicates the atomic dispersion of Fe on the support (Fig. S10g). Consistently, Fe K-edge EXAFS characterizations demonstrate the Fe–N<sub>4</sub> configuration of the single-atom Fe on the support (Fig. S9f, g, h, and i; Table S9).

### 3.3. Probing the catalytic reaction mechanism

The mechanistic insights behind the efficient BPA removal performance by Fe<sub>1</sub>-CN-BDA0.75 catalysis was then probed. First, we investigate the role of high-valent Fe(IV)=O species in the reaction system. Selective oxidation of methyl phenyl sulfoxide (MPSO) to methyl phenyl sulfone (MPSO<sub>2</sub>) via oxygen atom transfer reaction is one of the characteristic features of the high-valent Fe(IV)=O species [9,63–66]. MPSO

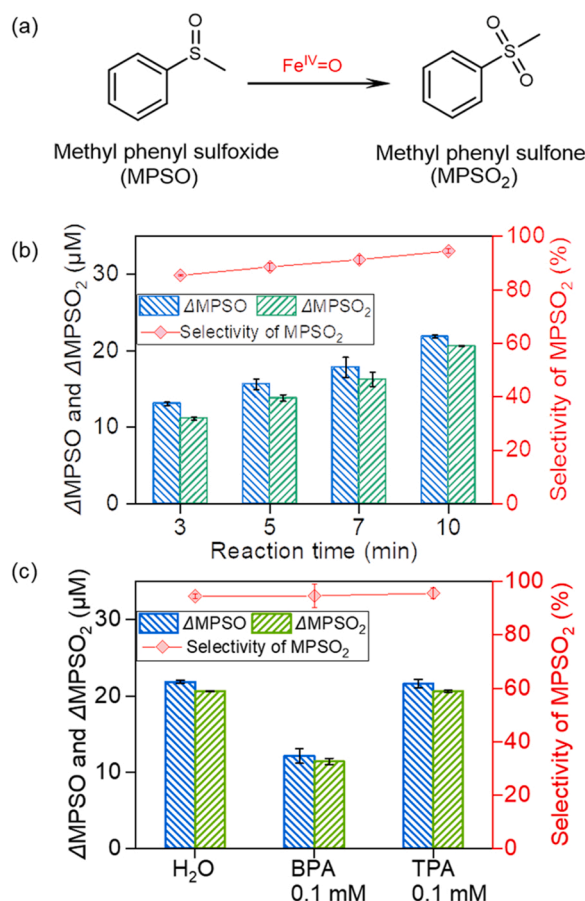


**Fig. 4.** Mechanistic investigations on the Fe<sub>1</sub>-CN-BDA0.75 catalyzed PMS activation reaction system. (a) Equation of the selective conversion of methyl phenyl sulfoxide (MPSO) to methyl phenyl sulfone (MPSO<sub>2</sub>) by high-valent Fe(IV)=O species. (b) Fe<sub>1</sub>-CN-BDA0.75 catalyzed selective conversion of MPSO to MPSO<sub>2</sub> in the presence of PMS. (c) MPSO to MPSO<sub>2</sub> conversion in the presence of BPA and TPA. Reaction conditions: [PMS] = 1.0 mM; [MPSO] = 0.1 mM.

to MPSO<sub>2</sub> conversion was thus employed to detect the Fe(IV)=O generated on the surface of Fe<sub>1</sub>-CN-BDA0.75 (Fig. 4a). As shown in Fig. 4b, Fe<sub>1</sub>-CN-BDA0.75 is active for selective MPSO to MPSO<sub>2</sub> conversion with a high MPSO<sub>2</sub> selectivity of 85–95%, confirming the generation of Fe(IV)=O in the reaction system. Nevertheless, the contribution of Fe(IV)=O in the pollutant degradation reaction must be elucidated. The pollutant molecules were thus introduced into the MPSO oxidation reaction system for observing the competition between the pollutant molecules and MPSO for the active-site of Fe(IV)=O. The presence of 0.1 mM BPA in the reaction system impedes the MPSO to MPSO<sub>2</sub> conversion, demonstrating that the Fe(IV)=O site is capable of oxidizing BPA (Fig. 4c). Additionally, TPA, which is proven to be stable in the Fe<sub>1</sub>-CN-BDA0.75 catalyzed reaction system, pose no impact on the selective MPSO to MPSO<sub>2</sub> conversion. Moreover, SCN<sup>−</sup> is a strong complex agent for the surface Fe sites, and could deactivate the Fe catalyzed reaction processes [67–69]. In the case of Fe<sub>1</sub>-CN-BDA0.75 catalyzed BPA degradation reaction, SCN<sup>−</sup> impedes the reaction completely (Fig. 5a), revealing that the pathway of Fe(IV)=O formation is blocked. These experimental facts reveal the significant contribution of the surface high-valent Fe(IV)=O species to the pollutant degradation.

Radicals, such as hydroxyl radical (•OH) and sulfate radical (SO<sub>4</sub>•<sup>−</sup>), are pervasive in various catalysis systems involving PMS. The possible contribution of the radical oxidation pathway to the BPA degradation was evaluated by quenching reactions and ESR spectroscopy technique. Owing to the high reaction rate constants, e.g.,  $k$  (•OH/CH<sub>3</sub>OH) =  $(1.2–2.8) \times 10^9 \text{ M}^{-1} \text{ s}^{-1}$ ,  $k$  (SO<sub>4</sub>•<sup>−</sup>/CH<sub>3</sub>OH) =  $(1.6–7.8) \times 10^7 \text{ M}^{-1} \text{ s}^{-1}$ , and  $k$  (•OH/TBA) =  $(3.8–7.6) \times 10^8 \text{ M}^{-1} \text{ s}^{-1}$  [70,71], methanol and tert-butyl alcohol (TBA) can readily react with hydroxyl and sulfate radicals. Meanwhile, in the presence of 500 mM of methanol and TBA ( $5 \times 10^3$  equivalent of the amount of BPA), no obvious attenuation of the BPA degradation reaction rate is observed. Therefore, the radical oxidation pathway is proposed to contribute negligible to the BPA degradation process. Further evidences on the contribution of the radicals come from the ESR measurement with 5,5-dimethyl-1-pyrroline N-oxide (DMPO) as the spin-trapping agent [72]. As shown in Fig. 5b, there is no signal recorded in the PMS aqueous solution without catalyst. The addition of catalyst in the reaction system leads to the appearance of a strong heptet peaks, which is the characteristic resonance signal of 5,5-dimethyl-2-pyrrolidone-N-oxyl ((DMPOX,  $a_N = 7.2 \text{ G}$ , and  $a_H = 4.1 \text{ G}$ ) [73]. As expected, the presence of 500 mM methanol and TBA in the reaction poses no impact on the intensities of the signal from DMPOX, excluding the DMPOX generation pathway through radical oxidation.

DMPOX could be generated via DMPO oxidation by singlet oxygen (<sup>1</sup>O<sub>2</sub>) [74]. In lieu of H<sub>2</sub>O, D<sub>2</sub>O was employed as the solvent to probe the contribution of <sup>1</sup>O<sub>2</sub> to DMPOX generation, since the decomposition reaction rate constant in H<sub>2</sub>O,  $k_d(\text{H}_2\text{O})$ , is  $2.5 \times 10^5 \text{ s}^{-1}$ , and  $k_d(\text{D}_2\text{O})$  is  $1.5 \times 10^5 \text{ s}^{-1}$ , i.e., <sup>1</sup>O<sub>2</sub> has a longer lifetime in D<sub>2</sub>O than in H<sub>2</sub>O [42,75]. However, the amplitude of the heptet signal is the same in the reaction system with D<sub>2</sub>O and H<sub>2</sub>O (Fig. 5b), excluding the contribution of the <sup>1</sup>O<sub>2</sub> to DMPOX generation. Together with the results of the MPSO conversion reactions, it is reasonable to proposed that DMPOX generation was initiated by Fe(IV)=O oxidation.

Furthermore, the probe reaction of DMPO conversion is correlated with the pollutant degradation reaction. The concentration of DMPOX generated on Fe<sub>1</sub>-CN-BDA0.75 is obviously higher than that on Fe<sub>1</sub>-CN, being consistent with the catalytic activity tests in BPA degradation reaction (Fig. 5c). In the presence of 0.1 mM BPA, the intensity of DMPOX signal is significantly reduced; however, the presence of 0.1 mM TPA pose negligible impact on the DMPOX generation. There data repeatedly demonstrate that Fe(IV)=O is the surface-active sites responsible for BPA and DMPO oxidation.

Afterwards, the possible contribution of the singlet oxygen is examined by ESR with 2,2,6,6-tetramethylpiperidine (TEMP) as the spin-trapping agent. As shown in Fig. 5d, the characteristic triplet signal reveals the formation of 2,2,6,6-tetramethylpiperidine-N-oxide

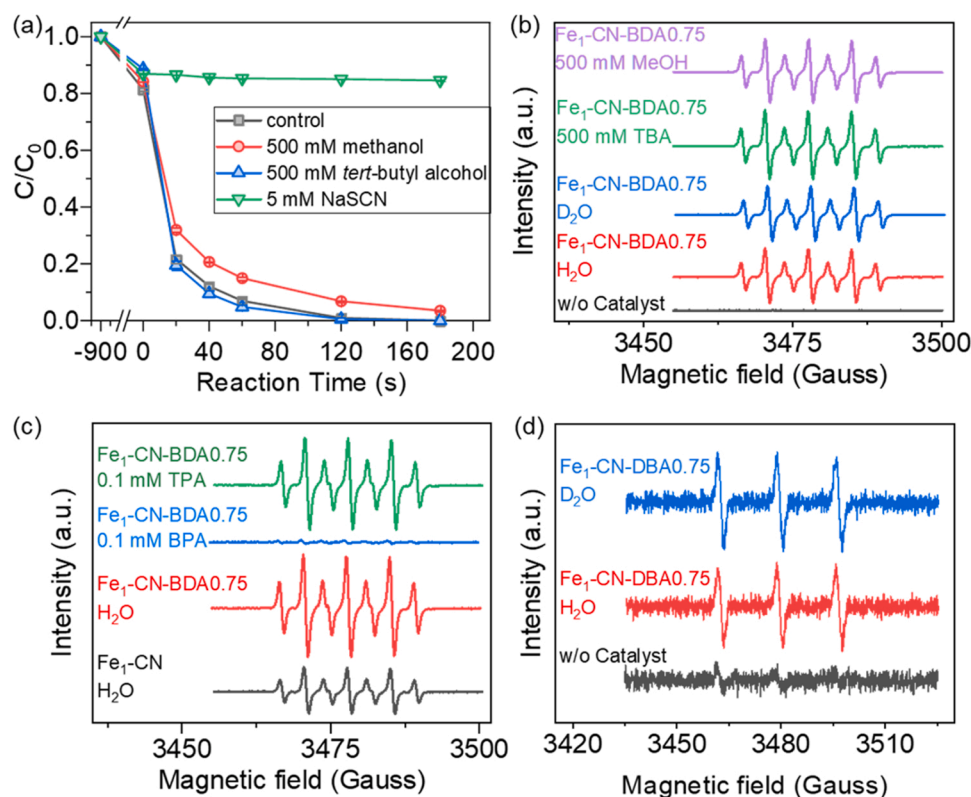


**Fig. 5.** (a) Quenching experiments. Reaction conditions: catalyst loading =  $0.20 \text{ g L}^{-1}$ ,  $[\text{PMS}] = 1.0 \text{ mM}$ ,  $[\text{BPA}] = 0.1 \text{ mM}$ ,  $[\text{TPA}] = 0.1 \text{ mM}$ ,  $[\text{MeOH}] = 500 \text{ mM}$ ,  $[\text{TBA}] = 500 \text{ mM}$ ,  $[\text{NaSCN}] = 10 \text{ mM}$ , and initial pH = 6.5. (b) Probing the possible contribution of the radicals in the reaction system by electron spin resonance (ESR) spectroscopy with 5,5-dimethyl-1-pyrroline N-oxide (DMPO) as the spin-trapping agent. (c) DMPOX signals impacted by the presence of BPA and TPA. (d) The impact of TPA on the DMPOX signal. (e) Analyzing the possible contribution of singlet oxygen in the reaction system with 2,2,6,6-tetramethylpiperidine (TEMP) as the spin-trapping agent.

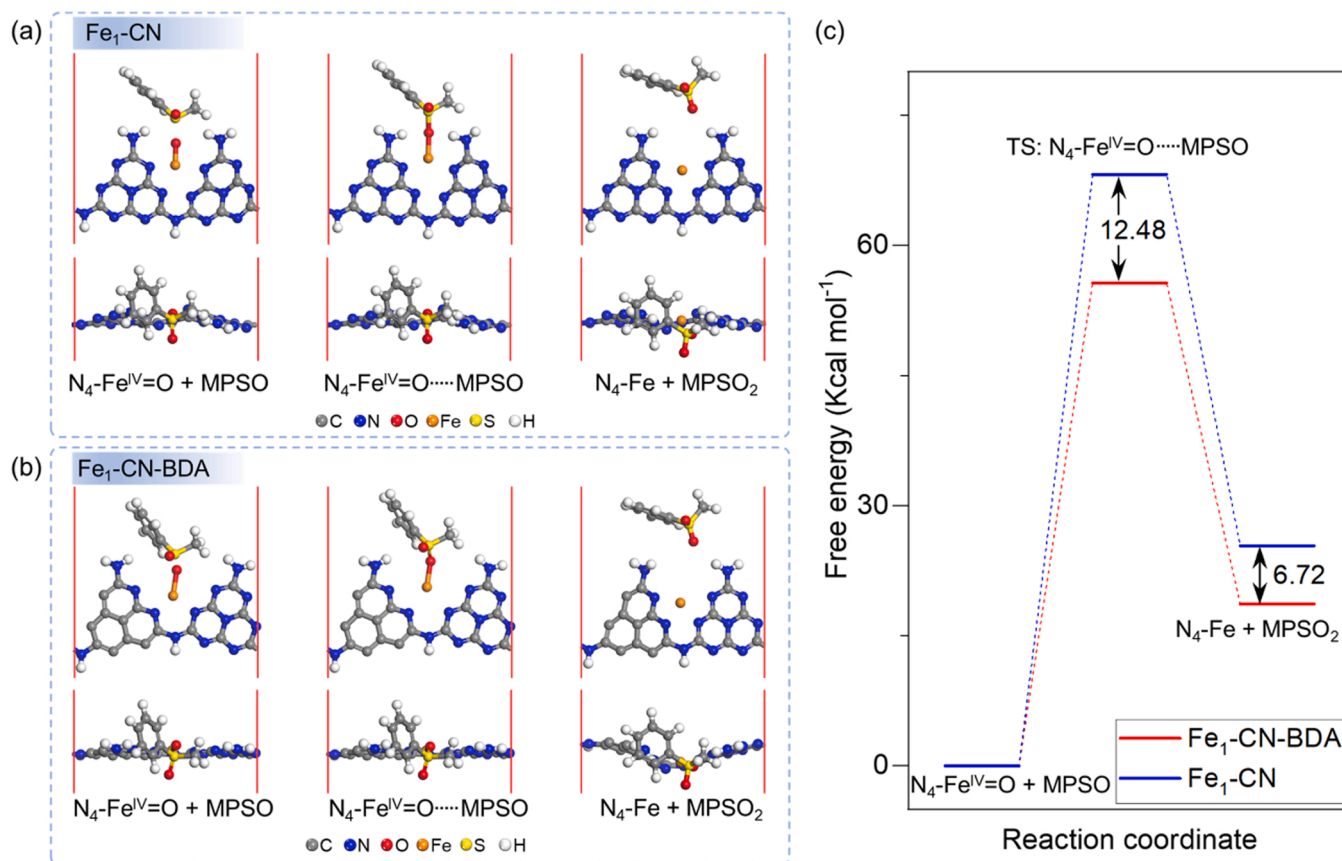


**Fig. 6.** Configuration of the initial, transition, and final states during MPISO to  $\text{MPISO}_2$  conversion via oxygen-atom transfer from  $\text{Fe}(\text{IV})=\text{O}$  species on  $\text{Fe}_1\text{-CN}$  (a) and  $\text{Fe}_1\text{-CN-BDA}$  (b). (c) Energy diagram of the oxygen-atom transfer reaction on  $\text{Fe}_1\text{-CN}$  and  $\text{Fe}_1\text{-CN-BDA}$ .

(TEMPO), revealing the possible existence of  $^1\text{O}_2$  in the reaction system. However, the expected enhancement of the triplet signal collected in  $\text{D}_2\text{O}$  is not observed, demonstrating that the triplet signal is produced via an alternative reaction mechanism, rather than  $^1\text{O}_2$  trapping by TEMP. TEMPO could be generated by a pathway involving one electron-oxidation of TEMP to  $\text{TEMP}^{\bullet+}$  (radical cation), deprotonation, and oxidation by dissolved oxygen [76,77]. The ESR analysis reveal the absence of  $^1\text{O}_2$  in the reaction system, and the high-valent  $\text{Fe(IV)=O}$  species is proposed to contribute to the TEMPO production.

Additionally, the variation in the concentration of PMS in the reaction system was analyzed for a further understanding of the reaction mechanism. Fig. S10 reveals the acceleration of PMS consumption by the presence of BPA in  $\text{Fe}_1\text{-CN-BDA0.75}$  catalyzed reaction system. The experimental fact is in line with reaction mechanism with the high-valent  $\text{Fe(IV)=O}$  as the dominant active species for BPA oxidation.

The mechanistic investigations together support a statement that the high-valent  $\text{Fe(IV)=O}$  plays the essential role in selective degradation of the pollutants. The conclusion herein motivated the further exploration on the question of how the activity of high-valent  $\text{Fe(IV)=O}$  species is determined by the configuration of the CN support. It is, however, difficult to experimentally probe the physicochemical properties of the transient high-valent  $\text{Fe(IV)=O}$  center on different CN supports. Computational quantum chemistry provides a platform that makes the simulation of the MSI possible [78]. Theoretical simulation was, thereafter, employed to investigate the thermal dynamics of oxygen-atom transfer from  $\text{Fe(IV)=O}$  to MPSP on CN support as well as on its carbon-rich counterpart. Fig. 6a and b show the configurations of the models for simulation. The CN support for  $\text{Fe}_1\text{-CN}$  is in a linear melon structure with repeating heptazine units. Replacing part of the N atoms with C atoms in the  $\text{Fe}_1\text{-CN}$  affords the model for  $\text{Fe}_1\text{-CN-BDA}$  with carbon-rich support. As shown in Fig. 6c, the energy barrier for generating the transition state of  $\text{N}_4\text{-Fe=O-MPSP}$  is significantly reduced by 12.48  $\text{Kcal mol}^{-1}$  by the configuration of carbon-richness. Meanwhile, the free energy of the final state of  $\text{FeN}_4 + \text{MPSP}_2$  on the carbon-rich  $\text{Fe}_1\text{-CN-BDA}$  is also 6.72  $\text{Kcal mol}^{-1}$  lower than that on  $\text{Fe}_1\text{-CN}$ . More favorable energy barriers of the oxygen-atom transfer reaction on carbon-rich CN framework as compared to the normal CN framework implicates higher reactivity of the high-valent  $\text{Fe(IV)=O}$  with the organic compounds. This could fundamentally contribute to the superior catalytic performance of  $\text{Fe}_1\text{-CN-BDA}$  in catalytic PMS activation for pollutant elimination.

#### 4. Conclusions

BDA involved polymerization generates carbon-rich CN framework. The structural engineering modulates the electronic properties of the conjugated CN framework, and thereby regulates the physicochemical properties of the single-atom Fe sites via MSI. The nature of carbon-richness of the support reduced the electron density of the single-atom Fe sites, and thus alters the thermal dynamics of the elemental reaction steps. The optimum catalyst,  $\text{Fe}_1\text{-CN-BDA0.75}$ , shows excellent performance in PMS activation for BPA degradation, which is 5.1 times of that with  $\text{Fe}_1\text{-CN}$ .  $\text{Fe}_1\text{-CN-BDA0.75}$  shows remarkable stability as demonstrated by the performance in a fixed-bed flow reactor. Systematic mechanistic analysis demonstrates the critical role of high-valent  $\text{Fe(IV)=O}$  species in BPA degradation. By theoretical simulation, the oxygen-atom transfer reaction is proven to be favorable on the high-valent  $\text{Fe(IV)=O}$  species supported by carbon-rich CN. The strategy of boosting the efficiency of single-atom catalyst via MSI regulation here is shedding light on developing highly-efficient single-atom catalysts for various applications.

#### CRediT authorship contribution statement

**Jiahao Cui:** Conceptualization, Methodology, Investigation, Writing – original draft. **Lina Li:** Methodology, Writing – review & editing.

**Yucheng Wu:** Investigation. **Jingyu Gao:** Investigation. **Kun Wang:** Investigation. **Caozheng Diao:** Methodology. **Chun Hu:** Writing – review & editing, Funding acquisition. **Yubao Zhao:** Conceptualization, Supervision, Project administration, Writing – review & editing.

#### Declaration of Competing Interest

The authors declare that they have no known competing financial interests or personal relationships that could have appeared to influence the work reported in this paper.

#### Data availability

Data will be made available on request.

#### Acknowledgment

Financial support from National Natural Science Foundation of China (21976041, 51838005) is acknowledged. The authors appreciate the XAS measurements from Singapore Synchrotron Light Source (SSLS) SUV (Soft X-Ray-Ultraviolet) Beamline and Shanghai Synchrotron Radiation Facility (SSRF) BL08U1-A Beamline.

#### Appendix A. Supporting information

Supplementary data associated with this article can be found in the online version at doi:10.1016/j.apcatb.2023.122706.

#### References

- [1] J. Wang, B. Li, Y. Li, X. Fan, F. Zhang, G. Zhang, W. Peng, *Adv. Sci.* 8 (2021), 2101824.
- [2] S. Shao, J. Cui, L. Li, M. Wang, P. Zhang, J. Cui, C. Hu, Y. Zhao, *RSC Adv.* 12 (2022) 5236–5244.
- [3] Y.-J. Zhang, G.-X. Huang, L.R. Winter, J.-J. Chen, L. Tian, S.-C. Mei, Z. Zhang, F. Chen, Z.-Y. Guo, R. Ji, Y.-Z. You, W.-W. Li, X.-W. Liu, H.-Q. Yu, M. Elimelech, *Nat. Commun.* 13 (2022) 3005.
- [4] X. Wu, J.-H. Kim, *ACS EST Engg.* (2022), <https://doi.org/10.1021/acsestengg.1022c00187>.
- [5] S. Liu, Q. Pan, J. Li, M. Wang, J. Zhang, Y. Song, C. Zhao, J. Shi, H. Deng, *ACS EST Water* 2 (2022) 817–829.
- [6] Y. Gao, Y. Zhu, Z. Chen, C. Hu, *ACS EST Engg.* 1 (2021) 76–85.
- [7] H. Dong, Y. Li, S. Wang, W. Liu, G. Zhou, Y. Xie, X. Guan, *Environ. Sci. Technol. Lett.* 7 (2020) 219–224.
- [8] F. Jacobsen, J. Holcman, K. Sehested, *Int. J. Chem. Kinet.* 30 (1998) 215–221.
- [9] B. Shao, H. Dong, B. Sun, X. Guan, *Environ. Sci. Technol.* 53 (2019) 894–902.
- [10] H. Li, C. Shan, B. Pan, *Environ. Sci. Technol.* 52 (2018) 2197–2205.
- [11] S. Shao, J. Cui, K. Wang, Z. Yang, L. Li, S. Zeng, J. Cui, C. Hu, Y. Zhao, *ACS EST Engg.* (2022), <https://doi.org/10.1021/acsestengg.1022c00236>.
- [12] E.S. Bernhardt, E.J. Rosi, M.O. Gessner, *Front. Ecol. Environ.* 15 (2017) 84–90.
- [13] V. Geissen, H. Mol, E. Klumpp, G. Umlauf, M. Nadal, M. van der Ploeg, S.E.A.T. M. van de Zee, C.J. Ritsema, *Int. Soil Water Conserv. Res.* 3 (2015) 57–65.
- [14] B. Liu, S.-g. Zhang, C.-C. Chang, *Water Environ. Res.* 92 (2020) 1603–1617.
- [15] Y. Tang, M. Yin, W. Yang, H. Li, Y. Zhong, L. Mo, Y. Liang, X. Ma, X. Sun, *Water Environ. Res.* 91 (2019) 984–991.
- [16] Y. Peng, W. Fang, M. Krauss, W. Brack, Z. Wang, F. Li, X. Zhang, *Environ. Pollut.* 241 (2018) 484–493.
- [17] W. Nam, *Acc. Chem. Res.* 40 (2007) 522–531.
- [18] Y.-M. Lee, S.N. Dhuri, S.C. Sawant, J. Cho, M. Kubo, T. Ogura, S. Fukuzumi, W. Nam, *Angew. Chem. Int. Ed.* 48 (2009) 1803–1806.
- [19] K.W. Kwong, D. Patel, J. Malone, N.F. Lee, B. Kash, R. Zhang, *N. J. Chem.* 41 (2017) 14334–14341.
- [20] J. Hohenberger, K. Ray, K. Meyer, *Nat. Commun.* 3 (2012) 720.
- [21] D. Menga, J.L. Low, Y.-S. Li, I. Arçon, B. Koyutürk, F. Wagner, F. Ruiz-Zepeda, M. Gaberšček, B. Paulus, T.-P. Fellinger, *J. Am. Chem. Soc.* (2021).
- [22] A. Mehmood, M. Gong, F. Jaouen, A. Roy, A. Zitolo, A. Khan, M.-T. Sougrati, M. Primbs, A.M. Bonastre, D. Fongalland, G. Drazic, P. Strasser, A. Kucernak, *Nat. Catal.* 5 (2022) 311–323.
- [23] Y. Zhou, G. Chen, Q. Wang, D. Wang, X. Tao, T. Zhang, X. Feng, K. Müllen, *Adv. Funct. Mater.* 31 (2021), 2102420.
- [24] F. Chen, X.-L. Wu, C. Shi, H. Lin, J. Chen, Y. Shi, S. Wang, X. Duan, *Adv. Funct. Mater.* 31 (2021), 2007877.
- [25] J. Yang, Z. Wang, C.-X. Huang, Y. Zhang, Q. Zhang, C. Chen, J. Du, X. Zhou, Y. Zhang, H. Zhou, L. Wang, X. Zheng, L. Gu, L.-M. Yang, Y. Wu, *Angew. Chem. Int. Ed.* 60 (2021) 22722–22728.
- [26] E. Zhao, M. Li, B. Xu, X.-L. Wang, Y. Jing, D. Ma, S. Mitchell, J. Pérez-Ramírez, Z. Chen, *Angew. Chem. Int. Ed.* 61 (2022), e202207410.



- [27] Z. Chen, E. Vorobyeva, S. Mitchell, E. Fako, N. López, S.M. Collins, R.K. Leary, P. A. Midgley, R. Hauert, J. Pérez-Ramírez, *Nat. Sci. Rev.* 5 (2018) 642–652.
- [28] R. Li, D. Wang, *Nano Res.* 15 (2022) 6888–6923.
- [29] F. Jaouen, E. Proietti, M. Lefèvre, R. Chenitz, J.-P. Dodelet, G. Wu, H.T. Chung, C. M. Johnston, P. Zelenay, *Energy Environ. Sci.* 4 (2011) 114–130.
- [30] C.T. Campbell, *Nat. Chem.* 4 (2012) 597–598.
- [31] Y. Shi, Z.-R. Ma, Y.-Y. Xiao, Y.-C. Yin, W.-M. Huang, Z.-C. Huang, Y.-Z. Zheng, F.-Y. Mu, R. Huang, G.-Y. Shi, Y.-Y. Sun, X.-H. Xia, W. Chen, *Nat. Commun.* 12 (2021) 3021.
- [32] G. Vilé, D. Albani, M. Nachtegaal, Z. Chen, D. Dontsova, M. Antonietti, N. López, J. Pérez-Ramírez, *Angew. Chem. Int. Ed.* 54 (2015) 11265–11269.
- [33] A. Akhundi, A. Zaker Moshfegh, A. Habibi-Yangjeh, M. Sillanpää, *ACS EST Engg.* 2 (2022) 564–585.
- [34] G. Zhang, Z.-A. Lan, X. Wang, *Angew. Chem. Int. Ed.* 55 (2016) 15712–15727.
- [35] W.-J. Ong, L.-L. Tan, Y.H. Ng, S.-T. Yong, S.-P. Chai, *Chem. Rev.* 116 (2016) 7159–7329.
- [36] V.S. Vyas, B.V. Lotsch, *Nature* 521 (2015) 41.
- [37] X. Wang, L. Chen, S.Y. Chong, M.A. Little, Y. Wu, W.-H. Zhu, R. Clowes, Y. Yan, M. A. Zwijnenburg, R.S. Sprick, A.I. Cooper, *Nat. Chem.* 10 (2018) 1180–1189.
- [38] Z. Chen, S. Mitchell, F. Krumeich, R. Hauert, S. Yakunin, M.V. Kovalenko, J. Pérez-Ramírez, *ACS Sustain. Chem. Eng.* 7 (2019) 5223–5230.
- [39] K. Sun, H. Shan, H. Neumann, G.-P. Lu, M. Beller, *Nat. Commun.* 13 (2022) 1848.
- [40] M. Shalom, S. Inal, C. Fettkenhauer, D. Neher, M. Antonietti, *J. Am. Chem. Soc.* 135 (2013) 7118–7121.
- [41] S.D. Richardson, S.Y. Kimura, *Anal. Chem.* 88 (2016) 546–582.
- [42] J. Cui, S. Shao, L. Li, P. Zhang, J. Cui, C. Hu, Y. Zhao, *ACS EST Engg.* 2 (2022) 2014–2022.
- [43] H. Yu, R. Shi, Y. Zhao, T. Bian, Y. Zhao, C. Zhou, G.I.N. Waterhouse, L.-Z. Wu, C.-H. Tung, T. Zhang, *Adv. Mater.* 29 (2017), 1605148.
- [44] X. Wang, K. Maeda, X. Chen, K. Takanabe, K. Domen, Y. Hou, X. Fu, M. Antonietti, *J. Am. Chem. Soc.* 131 (2009) 1680–1681.
- [45] X. Wang, K. Maeda, A. Thomas, K. Takanabe, G. Xin, J.M. Carlsson, K. Domen, M. Antonietti, *Nat. Mater.* 8 (2009) 76–80.
- [46] Y. Xiong, H. Li, C. Liu, L. Zheng, C. Liu, J.-O. Wang, S. Liu, Y. Han, L. Gu, J. Qian, D. Wang, *Adv. Mater.* 34 (2022), 2110653.
- [47] H. Gao, S. Yan, J. Wang, Y.A. Huang, P. Wang, Z. Li, Z. Zou, *Phys. Chem. Chem. Phys.* 15 (2013) 18077–18084.
- [48] P. Kumar, E. Vahidzadeh, U.K. Thakur, P. Kar, K.M. Alam, A. Goswami, N. Mahdi, K. Cui, G.M. Bernard, V.K. Michaelis, K. Shankar, *J. Am. Chem. Soc.* 141 (2019) 5415–5436.
- [49] J. Gu, C.-S. Hsu, L. Bai, H.M. Chen, X. Hu, *Science* 364 (2019) 1091–1094.
- [50] N. Zhang, T. Zhou, J. Ge, Y. Lin, Z. Du, Ca Zhong, W. Wang, Q. Jiao, R. Yuan, Y. Tian, W. Chu, C. Wu, Y. Xie, *Matter* 3 (2020) 509–521.
- [51] J.-R. Zhang, Y. Ma, S.-Y. Wang, J. Ding, B. Gao, E. Kan, W. Hua, *Phys. Chem. Chem. Phys.* 21 (2019) 22819–22830.
- [52] Y. Zheng, Y. Jiao, Y. Zhu, L.H. Li, Y. Han, Y. Chen, A. Du, M. Jaroniec, S.Z. Qiao, *Nat. Commun.* 5 (2014) 3783.
- [53] P. Leinweber, J. Kruse, F.L. Walley, A. Gillespie, K.-U. Eckhardt, R.I.R. Blyth, T. Regier, *J. Synchrotron Radiat.* 14 (2007) 500–511.
- [54] L.-S. Zhang, X.-Q. Liang, W.-G. Song, Z.-Y. Wu, *Phys. Chem. Chem. Phys.* 12 (2010) 12055–12059.
- [55] L. Yu, Y. Li, Y. Ruan, *Angew. Chem. Int. Ed.* 60 (2021) 25296–25301.
- [56] M. Wang, W. Yang, X. Li, Y. Xu, L. Zheng, C. Su, B. Liu, *ACS Energy Lett.* 6 (2021) 379–386.
- [57] C.-C. Hou, L. Zou, L. Sun, K. Zhang, Z. Liu, Y. Li, C. Li, R. Zou, J. Yu, Q. Xu, *Angew. Chem. Int. Ed.* 59 (2020) 7384–7389.
- [58] J. Li, Y.-f. Jiang, Q. Wang, C.-Q. Xu, D. Wu, M.N. Banis, K.R. Adair, K. Doyle-Davis, D.M. Meira, Y.Z. Finrock, W. Li, L. Zhang, T.-K. Sham, R. Li, N. Chen, M. Gu, J. Li, X. Sun, *Nat. Commun.* 12 (2021) 6806.
- [59] X. Xie, L. Peng, H. Yang, G.I.N. Waterhouse, L. Shang, T. Zhang, *Adv. Mater.* 33 (2021), 2101038.
- [60] Y. Pan, Y. Chen, K. Wu, Z. Chen, S. Liu, X. Cao, W.-C. Cheong, T. Meng, J. Luo, L. Zheng, C. Liu, D. Wang, Q. Peng, J. Li, C. Chen, *Nat. Commun.* 10 (2019) 4290.
- [61] H. Funke, A.C. Scheinost, M. Chukalina, *Phys. Rev. B* 71 (2005), 094110.
- [62] Q. Wang, Y. Yang, F. Sun, G. Chen, J. Wang, L. Peng, W.-T. Chen, L. Shang, J. Zhao, D. Sun-Waterhouse, T. Zhang, G.I.N. Waterhouse, *Adv. Energy Mater.* 11 (2021), 2100219.
- [63] Y. Zong, X. Guan, J. Xu, Y. Feng, Y. Mao, L. Xu, H. Chu, D. Wu, *Environ. Sci. Technol.* 54 (2020) 16231–16239.
- [64] Z. Wang, J. Jiang, S. Pang, Y. Zhou, C. Guan, Y. Gao, J. Li, Y. Yang, W. Qiu, C. Jiang, *Environ. Sci. Technol.* 52 (2018) 11276–11284.
- [65] Y. Zong, Y. Shao, Y. Zeng, B. Shao, L. Xu, Z. Zhao, W. Liu, D. Wu, *Environ. Sci. Technol.* 55 (2021) 7634–7642.
- [66] W. Nam, Y.-M. Lee, S. Fukuzumi, *Acc. Chem. Res.* 47 (2014) 1146–1154.
- [67] J. Li, W. Xia, J. Tang, Y. Gao, C. Jiang, Y. Jia, T. Chen, Z. Hou, R. Qi, D. Jiang, T. Asahi, X. Xu, T. Wang, J. He, Y. Yamauchi, *J. Am. Chem. Soc.* 144 (2022) 9280–9291.
- [68] Q. Wang, Z.-Y. Zhou, Y.-J. Lai, Y. You, J.-G. Liu, X.-L. Wu, E. Terefe, C. Chen, L. Song, M. Rauf, N. Tian, S.-G. Sun, *J. Am. Chem. Soc.* 136 (2014) 10882–10885.
- [69] Y. Mun, S. Lee, K. Kim, S. Kim, S. Lee, J.W. Han, J. Lee, *J. Am. Chem. Soc.* 141 (2019) 6254–6262.
- [70] J. Ma, N.J.D. Graham, *Water Res.* 34 (2000) 3822–3828.
- [71] L. Wang, H. Xu, N. Jiang, Z. Wang, J. Jiang, T. Zhang, *Environ. Sci. Technol.* 54 (2020) 4686–4694.
- [72] F.A. Villamena, in: F.A. Villamena (Ed.), *Reactive Species Detection in Biology*, Elsevier, Boston, 2017, pp. 163–202.
- [73] X. Li, X. Huang, S. Xi, S. Miao, J. Ding, W. Cai, S. Liu, X. Yang, H. Yang, J. Gao, J. Wang, Y. Huang, T. Zhang, B. Liu, *J. Am. Chem. Soc.* 140 (2018) 12469–12475.
- [74] P. Bilski, K. Reszka, M. Bilka, C.F. Chignell, *J. Am. Chem. Soc.* 118 (1996) 1330–1338.
- [75] F. Wilkinson, W.P. Helman, A.B. Ross, *J. Phys. Chem. Ref. Data* 24 (1995) 663–677.
- [76] E.-T. Yun, J.H. Lee, J. Kim, H.-D. Park, J. Lee, *Environ. Sci. Technol.* 52 (2018) 7032–7042.
- [77] G. Nardi, I. Manet, S. Monti, M.A. Miranda, V. Lhiaubet-Vallet, *Free Radic. Biol. Med.* 77 (2014) 64–70.
- [78] J.K. Nørskov, T. Bligaard, J. Rossmeisl, C.H. Christensen, *Nat. Chem.* 1 (2009) 37–46.